Seismic attenuation and velocity dispersion in heterogeneous partially saturated porous rocks

J. Germán Rubino and Klaus Holliger

Institute of Geophysics, University of Lausanne, CH-1015 *Lausanne, Switzerland. E-mail: german.rubino@unil.ch*

SUMMARY

Using a numerical approach, we explore wave-induced fluid flow effects in partially saturated porous rocks in which the gas–water saturation patterns are governed by mesoscopic heterogeneities associated with the dry frame properties. The link between the dry frame properties and the gas saturation is defined by the assumption of capillary pressure equilibrium, which in the presence of heterogeneity implies that neighbouring regions can exhibit different levels of saturation. To determine the equivalent attenuation and phase velocity of the synthetic rock samples considered in this study, we apply a numerical upscaling procedure, which permits to take into account mesoscopic heterogeneities associated with the dry frame properties as well as spatially continuous variations of the pore fluid properties. The multiscale nature of the fluid saturation is taken into account by locally computing the physical properties of an effective fluid, which are then used for the larger-scale simulations. We consider two sets of numerical experiments to analyse such effects in heterogeneous partially saturated porous media, where the saturation field is determined by variations in porosity and clay content, respectively. In both cases we also evaluate the seismic responses of corresponding binary, patchy-type saturation patterns. Our results indicate that significant attenuation and modest velocity dispersion effects take place in this kind of media for both binary patchy-type and spatially continuous gas saturation patterns and in particular in the presence of relatively small amounts of gas. The numerical experiments also show that the nature of the gas distribution patterns is a critical parameter controlling the seismic responses of these environments, since attenuation and velocity dispersion effects are much more significant and occur over a broader saturation range for binary patchy-type gas–water distributions. This analysis therefore suggests that the physical mechanisms governing partial saturation should be accounted for when analysing seismic data in a poroelastic framework. In this context, heterogeneities associated with the dry frame properties, which do not play important roles in wave-induced fluid flow processes *per se*, should be taken into account since they may determine the kind of gas distribution pattern taking place in the porous rock.

Key words: Permeability and porosity; Seismic attenuation; Computational seismology; Theoretical seismology; Wave propagation; Acoustic properties.

1 INTRODUCTION

The classical version of the theory of poro-elasticity (Biot 1956a,b) assumes that wave-induced fluid movements at the macroscopic scale, as defined by the prevailing wavelengths, are the only causes of seismic velocity dispersion and attenuation in porous media. Correspondingly, the probed material is supposed to be homogeneous at submacroscopic scales and all elastic moduli are real-valued and independent of frequency. However, there is consistent evidence to demonstrate that, on its own, this physical mechanism is unable to fully account for the intrinsic attenuation behaviour inferred from seismic observations in sedimentary environments and that

other energy loss mechanisms play crucial roles (Pride *et al.* 2004). Notably, there is increasing evidence indicating that the presence of heterogeneity in the mesoscopic scale range, that is, inhomogeneities larger than the pore size but smaller than the prevailing wavelengths, may be capable of explaining the observed attenuation levels at seismic frequencies (e.g. Pride *et al.* 2004; Müller *et al.* 2010). These mesoscopic heterogeneities may be associated with the nature and composition of the pore fluids and/or the dry frame properties of the rock. The corresponding loss mechanism is then governed by fluid pressure equilibration taking place between the different mesoscopic regions composing the heterogeneous porous medium. For this reason, this loss mechanism is sensitive to physical

parameters of great interest, such as porosity (Gurevich & Lopatnikov 1995; Pride *et al.* 2004), permeability (Müller *et al.* 2007; Rubino *et al.* 2009), type of pore fluids, degree of saturation and fluid spatial distribution (Müller *et al.* 2008; Rubino *et al.* 2009; Toms-Stewart *et al.* 2009; Rubino *et al.* 2011).

The presence of so-called patchy gas-water saturation, that is, spatially variable gas–water distributions in the form of local patches fully saturated with gas embedded in regions fully saturated with water, can produce very significant attenuation and velocity dispersion effects (e.g. Rubino *et al.* 2009). This is due to the very high compressibility of gas as compared with that of water, which in the presence of favourable gas patch geometries and seismic frequencies can lead to significant fluid pressure gradients and thus to the enhancement of corresponding mesoscopic effects. That is why binary patchy-type saturation received great interest from the researchers during the last decades, who aimed at linking these potentially observable effects with various pertinent petrophysical parameters, such as saturation, porosity and permeability. In fact, White and coauthors (White 1975; White *et al.* 1975) were the first to propose the presence of mesoscopic heterogeneities as an important seismic attenuation mechanism and analysed the case of plane porous layers alternately saturated with gas and water (White *et al.* 1975) as well as of spherical gas pockets in a water-saturated porous rock (White 1975). After these pioneering works, a number of authors have made important contributions to a better understanding of this subject using a variety of methods. For instance, Dutta & Odé (1979) analysed mesoscopic effects related to porous rocks containing spherical gas pockets, as defined in White's (1975) model, in the framework of Biot's (1956a) theory. Norris (1993) developed a theory for low-frequency attenuation and dispersion of compressional waves in heterogeneous fluid-saturated layered materials and focused on the case of patchy saturation. The case of gas patches of arbitrary geometries was analysed by Johnson (2001), who proposed the simplest function for the dynamic bulk modulus that ensured causality of the solution to describe the crossover from Gassmann-Wood's bound at low frequencies to the Gassmann-Hill bound at high frequencies. Müller & Gurevich (2005) developed a theory for estimating wave attenuation and dispersion in a porous medium containing a random distribution of 3D heterogeneities characterized by small contrasts in their physical properties. Later, Toms *et al.* (2006) extended the model proposed by Müller & Gurevich (2005) to the case of partial saturation in conjunction with arbitrary contrasts of the fluid bulk modulus and a homogeneous rock frame. Recently, Masson & Pride (2011) analysed seismic attenuation produced by patchy saturation in homogeneous dry frames considering numerically generated fluid distribution patterns obtained using the invasion-percolation model. These authors also studied the effects of spatial fluctuations in the fluid saturation over multiple scales, considering voxels locally saturated with either water or gas (Masson & Pride 2011).

Most researchers analysing seismic attenuation and velocity dispersion due to the presence of gas–water distributions consider mesoscopic zones fully saturated with gas surrounded by regions fully saturated with water and do not consider potential physical reasons for the existence of such patchy saturation. However, depending on how partial saturation is obtained, there are physical reasons that render the existence of binary gas–water distributions unlikely. For instance, during drainage experiments, where a gaseous phase displaces a liquid one, there is always some residual water saturation present in the pore space (e.g. Dvorkin *et al.* 1999). In addition, as stated by Toms *et al.* (2006), in real rocks gas patches are expected to be characterized by a broad distribution of shapes and sizes. Given

that the effects of very small patches can be properly described by Gassmann-Wood model, partially saturated media should therefore be considered as a porous frame saturated with a composite fluid with smoothly varying physical properties (Toms *et al.* 2006). The available evidence from laboratory experiments also rather point to spatially continuous variations of the gas saturation in partially saturated porous media (Cadoret *et al.* 1995; Cadoret *et al.* 1998; Toms-Stewart *et al.* 2009). Moreover, as stated by Knight *et al.* (1998) and Dvorkin & Nur (1998), non-uniform saturation patterns may result from textural and/or mineralogical heterogeneities under conditions of capillary pressure equilibrium. Because within a given lithological unit rock frame heterogeneities are expected to be spatially continuous, gas saturation fields are expected to be spatially continuous as well. To our knowledge, however, little work has so far been done to study in detail the role of smoothly spatially varying properties of the fluid phase in partially saturated porous media with regard to the attenuation and dispersion behaviour of seismic wavefields. The corresponding analysis is quite complex as both heterogeneities associated with the dry matrix properties as well as with spatially continuous variations of gas saturation need to be simultaneously accounted for. A recent effort in this direction was presented by Toms *et al.* (2006) who modelled the influence on acoustic properties of fluid distribution patterns having continuous spatial variations of the bulk modulus. These authors considered a homogeneous rock frame partially saturated with water and gas. The corresponding fluid distributions were determined by submillimetre resolution X-ray tomographic images obtained during gas injection laboratory experiments.

In this work, we analyse wave-induced fluid flow effects in numerical porous rock samples partially saturated with gas and water, where the saturation patterns are governed by mesoscopic heterogeneities associated with the dry frame properties. To this end, we consider the model by Knight *et al.* (1998) to obtain the corresponding gas saturation fields from the distributions of dry frame properties and capillary pressure. Through an upscaling procedure based on numerical compressibility tests (Rubino *et al.* 2009) we then compute the attenuation and velocity dispersion behaviour associated with the considered mesoscopic heterogeneities in the seismic range of frequencies. This methodological framework thus allows us to systematically explore wave-induced fluid flow effects in heterogeneous partially saturated media, where the saturation field is governed by heterogeneous distributions of the porosity and clay content, respectively.

2 PHYSICAL MODEL FOR POROUS ROCKS PARTIALLY SATURATED WITH GAS AND WATER

The spatial characteristics of gas–water saturation patterns depend on rock heterogeneities, the prior history of fluid movement, and viscous effects, such as viscous fingering (Homsy 1987). Several authors have used X-ray tomography to visualize the fluid distributions in porous rocks and have found that the shape and distribution of the fluid phases depends on the overall saturation, that is, on the fraction of the total pore volume occupied by gas in the sample as well as on the process of fluid saturation (Cadoret *et al.* 1995; Cadoret *et al.* 1998; Toms-Stewart *et al.* 2009). Cadoret *et al.* (1998) show that imbibition experiments within an 8 cm diameter rock sample, where the liquid phase displaces the gaseous one, produce fluid distributions which are homogeneous at the millimetre scale. Conversely, drainage experiments, where the opposite procedure is performed, produce gas clusters or patches and satu-

ration can be considered heterogeneous at the corresponding meso-scopic scales. Cadoret *et al.* (1995) repeated drainage experiments on a given slice of rock to obtain a certain overall gas saturation. They were able to observe the same patterns of gas bearing regions invading the water-saturated sample showing the reproducibility of the saturation fields obtained with this technique. Moreover, these experiments show that saturation patterns resulting from drainage experiments are mainly controlled by the intrinsic textural properties of the considered rock samples.

Knight *et al.* (1998) and Dvorkin & Nur (1998) demonstrated that the heterogeneous nature of porous rocks often results in correspondingly heterogeneous saturation distributions on scales greater than the pore size. Thus, if we are interested in a detailed analysis of wave-induced fluid flow effects in partially saturated porous media, such heterogeneities associated with the dry frame properties should be considered in conjunction with the corresponding spatially continuous gas saturation field. Following Knight *et al.* (1998), we determine the gas–water distribution of heterogeneous rock samples by assuming a state of capillary equilibrium ignoring gravitational forces. We therefore assume that capillary pressure everywhere is constant, which in turn implies that neighbouring regions with different textural and/or mineralogical properties exhibit different levels of saturation. To do so, we link the level of water saturation S_w to the capillary pressure P_c using the relationship of Brooks & Corey (1964)

$$S_w = S_r + (1 - S_r)\left(\frac{P_t}{P_c}\right)^\lambda,   (1)$$

where S_r is the irreducible water saturation, λ is a constant for each lithology and P_t is the threshold pressure, that is, the minimum pressure needed to initiate the displacement of a wetting phase by a non-wetting phase from a porous medium fully saturated with the wetting phase (Thomas *et al.* 1968). Again following Knight *et al.* (1998), we also link the threshold pressure to permeability through the empirical relation proposed by Thomas *et al.* (1968)

$$P_t = 52\kappa^{-0.43},   (2)$$

where the pressure P_t is in units of KPa and the permeability κ in mD. Eqs (1) and (2) allow for obtaining the water saturation as a function of permeability and capillary pressure at any given location of our models.

To analyse wave-induced fluid flow effects associated with realistic partial gas–water distributions, we consider highly heterogeneous spatially continuous variations of the dry frame properties of the rock samples. Then, we determine for different capillary pressure values, the corresponding gas saturation fields using eqs (1) and (2) and use the numerical upscaling procedure proposed by Rubino *et al.* (2009) to quantify the corresponding attenuation and velocity dispersion due to wave-induced fluid flow. For completeness, we outline the key aspects of this approach in the Appendix. Please note that, although we assume that capillary pressure determines the fluid distributions in the considered rock samples, we do not take into account this parameter when determining the response of samples subjected to the compressibility test.

Even though gas and water are immiscible fluids, we must consider at every computational cell composing the numerical rock sample under study, a single-phase effective fluid. The reason for this is that our upscaling procedure is based on Biot's (1956a) theory and thus does not support the presence of two pore fluids. The density of the equivalent fluid is given by

$$\rho_f = S_g\rho_g + S_w\rho_w,   (3)$$

where $S_g = (1 - S_w)$ is the gas saturation and ρ_g and ρ_w are the densities of the gas and water, respectively. The compressibility of the effective fluid is a critical parameter in the analysis of wave-induced fluid flow effects. However, if the cell size is smaller than the diffusion lengths involved in the analysis, as is indeed the case for all models considered in this study, the characteristic sizes of the gas patches that may exist within such cell will also be much smaller than the diffusion lengths. Hence, there is enough time for the fluid pressure to equilibrate and the fluid pressure is uniform. Consequently, regardless of the geometry of the distribution of gas and water within a particular cell, we can use Wood's (1955) law to obtain the bulk modulus of the equivalent fluid

$$\frac{1}{k_f} = \frac{S_g}{k_g} + \frac{S_w}{k_w},   (4)$$

where k_g and k_w are the bulk modulus of the gas and water, respectively. Following Carcione *et al.* (2006) we then use the relation of Teja & Rice (1981) to obtain the viscosity of the two-phase fluid mixture

$$\eta_f = \eta_g\left(\frac{\eta_w}{\eta_g}\right)^{S_w},   (5)$$

where η_g and η_w denote the viscosities of gas and water, respectively.

3 PARTIAL SATURATION INDUCED BY POROSITY VARIATIONS

Spatial variations in porosity affect the corresponding permeability field, and thus, in the framework of the physical model outlined above, generate heterogeneous gas–water saturation patterns, which in turn can produce significant seismic attenuation and velocity dispersion effects. We assume that the rock frame is composed of quartz grains with the physical properties given in Table 1 and consider heterogeneous porosity distributions. In addition to changes in permeability, variations in porosity also imply changes in other

Table 1. Material properties for the models considered in this study.

	Solid phase			
	Density (g cm^{-3})	Bulk modulus (GPa)	Shear modulus (GPa)	Mean grain diameter (m)
Quartz	$\rho_q = 2.65$ [a]	$k_q = 37$ [a]	$\mu_q = 44$ [a]	$d_q = 8 \times 10^{-5}$ [b]
Clay	$\rho_c = 2.55$ [a]	$k_c = 25$ [a]	$\mu_c = 9$ [a]	
	Fluid phase			
	Density (g cm^{-3})	Bulk modulus (GPa)	Viscosity (P)	
Water	$\rho_w = 1.04$ [a]	$k_w = 2.25$ [a]	$\eta_w = 0.03$ [a]	
Gas	$\rho_g = 0.078$ [a]	$k_g = 0.012$ [a]	$\eta_g = 0.0015$ [a]	

The parameters were taken from [a]Mavko *et al.* (2009) and [b]Rubino *et al.* (2009).

physical parameters, such as frame moduli and bulk density. At each computational cell, the bulk density is given by

$$\rho_b = (1 - \phi)\rho_q + \phi\rho_f, \qquad (6)$$

where ϕ denotes porosity and ρ_q is the density of quartz.

We use the Kozeny-Carman equation to relate the porosity ϕ and the mean grain diameter d_q of the rock sample to the permeability κ (e.g. Mavko *et al.* 2009)

$$\kappa = B \frac{\phi^3}{(1 - \phi)^2} d_q^2, \qquad (7)$$

where B is a geometric factor that depends on the tortuosity of the porous sample.

To link the porosity ϕ and the solid grain properties with the elastic moduli of the dry frame we use the model of Krief *et al.* (1990)

$$k_m = k_s(1 - \phi)^{4/(1-\phi)}, \qquad (8)$$

$$\mu_m = k_m\mu_s/k_s, \qquad (9)$$

where k_s and μ_s are the bulk and shear moduli of the solid grains, respectively, and k_m and μ_m are the corresponding parameters of the solid frame.

3.1 Effective single-phase fluid

Before analysing heterogeneous porosity distributions and associated partial gas saturation patterns, we study the response of rock samples containing patches fully saturated with gas in contact with regions fully saturated with water. In doing so, we assume that the corresponding gas patches are much smaller than the diffusion lengths involved in these experiments. We do this to verify the basic validity of considering an effective fluid in general and the applicability of eqs (3)–(5) to represent the regions of the model containing the heterogeneous gas–water distributions in particular.

In this sense, we consider a rectangular rock sample that is 0.5 m high and 0.1 m wide and composed of three layers with thicknesses of 0.1 m, 0.05 m and 0.35 m (Fig. 1). The thickest layer is fully saturated with water, while the thinnest one is partially saturated with gas and water. In the latter, the two immiscible fluids are present in very small patches, fully saturated with gas or water, with an overall gas saturation of 0.21. The remaining layer also contains very small patches fully saturated with gas in contact with regions fully saturated with water and has an overall gas saturation of 0.55. For the physical properties of gas and water we take the values shown in Table 1.

We use eq. (7) with $B = 0.003$ (Carcione & Picotti 2006) to compute the permeability of the rock samples and, in all experiments presented in this paper, we assume $\lambda = 0.9$ and $S_r = 0.05$ to obtain the gas saturation as function of permeability according to eqs (1) and (2). For this particular experiment we also assume that the dry frames of each one of the three layers are homogeneous and, after selecting a value for the capillary pressure, we determine the corresponding porosity ϕ according to the partial saturation model detailed in the previous section. Thus, we consider $\phi = 0.33$ for the region containing the highest overall gas saturation, $\phi = 0.15$ for the fully saturated layer, and $\phi = 0.21$ for the remaining zone. Finally, we use the eqs (8) and (9) to calculate the elastic moduli of the dry frame of the different regions.

The diffusion length for the different media composing the rock sample is given by
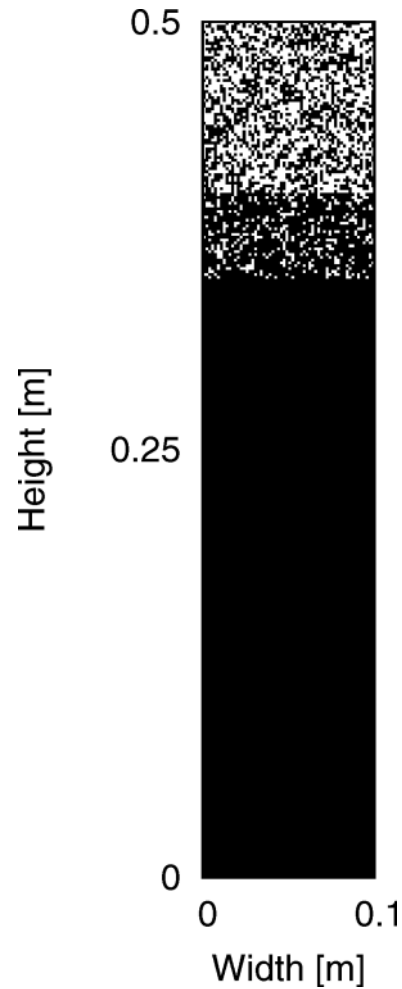
$$L_d = \sqrt{D/\omega}, \qquad (10)$$

Figure 1. Layered model containing heterogeneous patchy gas–water distributions considered to analyse the validity of our effective single-phase fluid approximation. White regions are fully saturated with gas, while black ones are fully saturated with water.

where ω is the angular frequency and D is the diffusivity defined as (e.g. Pride 2005)

$$D = \frac{\kappa}{\eta_f}\left(\frac{M_c k_{av} - \alpha^2 k_{av}^2}{M_c}\right). \qquad (11)$$

The parameters M_c, k_{av} and α can be computed in terms of the physical properties of the fluid-saturated porous media as follows (Rubino *et al.* 2009):

$$\alpha = 1 - \frac{k_m}{k_s}, \qquad (12)$$

$$k_{av} = \left(\frac{\alpha - \phi}{k_s} + \frac{\phi}{k_f}\right)^{-1}, \qquad (13)$$

$$M_c = k_m + \alpha^2 k_{av} + \frac{4}{3}\mu, \qquad (14)$$

where μ is the shear modulus of the fluid-saturated porous rock taken to be equal to the shear modulus of the dry frame.

We have calculated the diffusion lengths for the different regions composing the three layers considered in the model shown in Fig. 1 using eqs (10) and (11) and verified that the smallest diffusion length $L_d = 1.35$ cm occurs for $\phi = 0.21$ at the regions fully saturated with
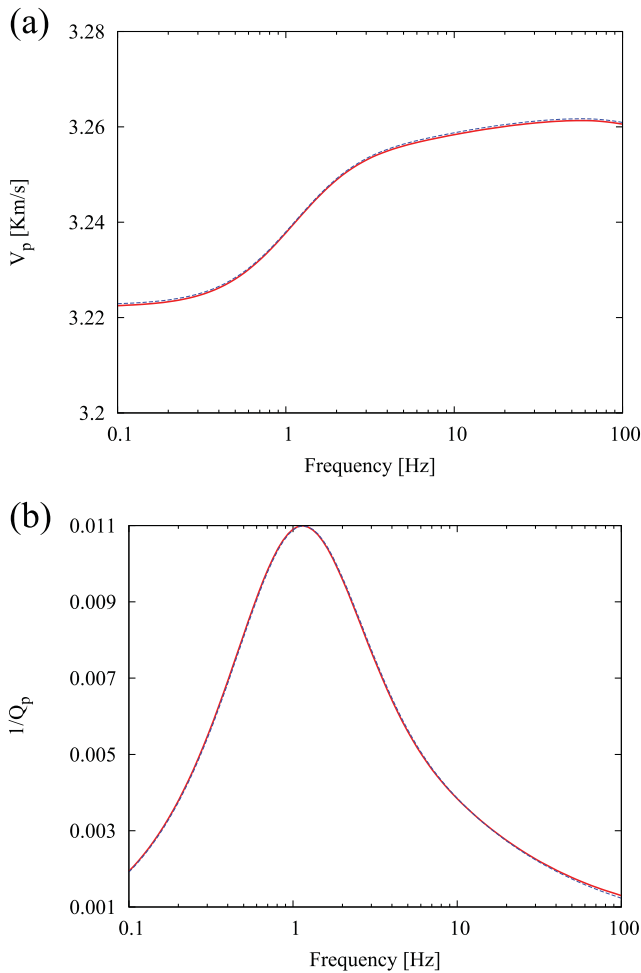
Figure 2. (a) Equivalent phase velocity and (b) inverse quality factor as functions of frequency obtained using the numerical upscaling procedure outlined in the Appendix and considering heterogeneous patchy gas–water distributions (red lines). This plot also shows the corresponding response obtained using the same procedure but replacing the horizontal regions by homogeneous porous layers containing an effective single-phase fluid (blue lines).

gas and for the highest frequency considered in this work (100 Hz). In addition, in the layer with $\phi = 0.33$, the diffusion length turned out to be smallest ($L_d = 2.4$ cm) for zones fully saturated with gas and for a frequency of 100 Hz. We thus observe that the fluid patches in the different layers have characteristic sizes smaller than the corresponding diffusion lengths. Please note that the grid spacing used for the corresponding numerical simulations is 0.17 cm.

Figs 2(a) and (b) show the equivalent phase velocity and the inverse quality factor as functions of frequency obtained using the numerical upscaling procedure. These plots also show the corresponding responses when replacing the layers containing the heterogeneous patchy gas–water distributions by homogeneous porous layers containing corresponding effective single-phase fluids with properties given by eqs (3)–(5) computed according to the corresponding overall gas saturation of the layer. We observe excellent agreement between the two responses, which in turn suggests that the effective single-phase fluid with average properties can be used to adequately represent heterogeneous patchy gas–water distributions as long as the characteristic size of the patches is smaller than the involved diffusion lengths. Since in the experiments considered

in this paper the grid spacing was chosen on the order of or smaller than the involved diffusion lengths, the characteristic sizes of the gas patches that could be located within a given computational cell are expected to be smaller than such lengths. An effective single phase fluid characterized by the eqs (3)–(5) can therefore be considered to adequately represent the behaviour of the two immiscible fluids located within the pore space of such region.

3.2 Partial gas saturation associated with heterogeneous porosity distributions

In the following, we shall explore the effects of partial saturation due to realistic, heterogeneous porosity distributions. To do so, we consider a von-Karman-type spectral density function of the form

$$S_d(k_x, k_y) = S_0 \left(1 + k_x^2 a_x^2 + k_y^2 a_y^2\right)^{-(H+E/2)}, \qquad (15)$$

where k_x and k_y are the horizontal and vertical wavenumbers, a_x and a_y are the horizontal and vertical correlation lengths, S_0 is a normalization constant and E is the Euclidean dimension. The exponent H varies between 0 and 1 and determines the roughness and complexity of the considered stochastic process (e.g. Tronicke & Holliger 2005). This expression corresponds to a band-limited scale-invariant stochastic process with a Hausdorff fractal dimension $D_H = E + 1 - H$.

To generate heterogeneous porosity fields with corresponding characteristics, we first partition the computational domain into a finite number of grid cells Ω_j and assign to each of these cells a pseudo-random number drawn from a uniform distribution. Then, we Fourier transform this field to the spatial wavenumber domain and filter its amplitude spectrum using the eq. (15). Finally, we transform back the result to the spatial domain to obtain the heterogeneous field.

Fig. 3 shows the particular porosity field employed in the analysis, which has a mean of 0.3 and standard deviation of 0.029, and was obtained considering a spatially isotropic correlation length of 0.1 m and $H = 0.1$. Please note that this choice of H emulates the ubiquitous and seemingly universal flicker noise character observed for porosity log data (e.g. Kelkar & Perez 2002). The grid spacing considered in this case is of 0.005 m, which is much smaller than the involved diffusion lengths. This can be verified in Fig. 4, where we show the diffusion length as a function of porosity for a frequency of 100 Hz. To compute this parameter, we consider the model presented in this section for the two limiting fluid
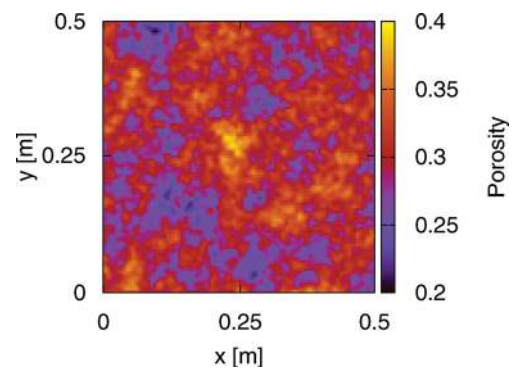

Figure 3. Heterogeneous porosity field considered to analyze seismic attenuation and velocity dispersion associated with corresponding partial gas–water saturation. This field has a mean of 0.3 and a standard deviation of 0.029.
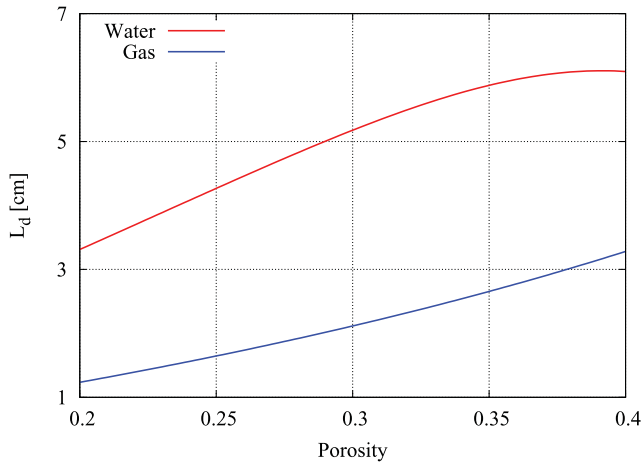
Figure 4. Diffusion length as a function of porosity for a frequency of 100 Hz considering full water and full gas saturation.

cases: full water and full gas saturation. The corresponding results show that the diffusion length increases with porosity and can be as small as about 1 cm in these environments, mainly for very low porosity. We also see that the diffusion length is smaller when the rock sample is fully saturated with gas. Moreover, eq. (10) suggests that the diffusion length is expected to increase with decreasing frequency.

Fig. 5 shows, for different capillary pressure values, gas saturation fields for the porosity model shown in Fig. 3 as predicted by eqs (1) and (2). The overall gas saturations of these samples, defined as

$$\overline{S}_{g} = \frac{\sum_j S_g(\Omega_j)\phi(\Omega_j)}{\sum_j \phi(\Omega_j)}, \qquad (16)$$

with Ω_j denoting the jth cell in the grid, are (a) 0.00023, (b) 0.002, (c) 0.0085 and (d) 0.023.

We observe that when capillary pressure is relatively low only the most permeable regions of the sample contain some gas within the pore spaces (Fig. 5). In fact, it is important to note here that in the extreme case shown in Fig. 5(a) the fluid distribution does not seem to be statistically representative. This is due to the fact that in this case the capillary pressure is very low and, correspondingly, the amount of gas in the sample is extremely small ($S_g = 0.00023$) and therefore only a very small region characterized by very high porosity contains some gas. As capillary pressure increases, the low permeability regions start to contain some gas and, thus, the fields shown in Figs 5(b)–(d) become increasingly statistically representative.

Figs 6 and 7 show the equivalent inverse quality factor and compressional phase velocity as functions of frequency for the porosity distribution shown in Fig. 3 and the corresponding saturation patterns displayed in Fig. 5. We observe that significant attenuation can take place, mainly in cases (c) and (d), with Q-values below 50 for certain frequencies. In case (a) attenuation is negligible with Q-values above 400 for the frequencies considered in this analysis. In case (b), Q takes values below 100 for frequencies above 30 Hz. On the other hand, we observe that velocity dispersion is not significant with relative changes of less than 1.5 per cent in the considered frequency range.

To analyse the role played by the spatially continuous nature of gas–water distributions, we also include in this analysis the responses of patchy-type binary gas–water distributions obtained from the saturation fields shown in Fig. 5. To do so, we assume a certain threshold saturation value S_t, and for each cell we modify the saturation so that for those having $S_g \leq S_t$ we change the gas saturation to zero, and on the contrary, if $S_g > S_t$ we consider that the corresponding cell is fully saturated with gas. We choose the threshold value according to the behaviour of the bulk modulus of the mixture of gas and water, since this physical property is a key parameter controlling wave-induced fluid flow in this kind of media. In the numerical experiments, we choose for the threshold value
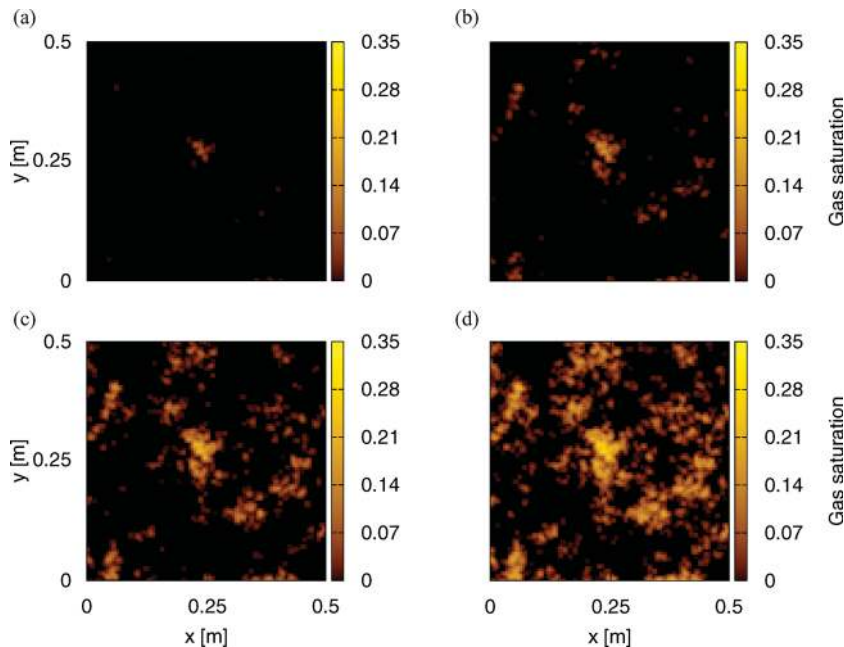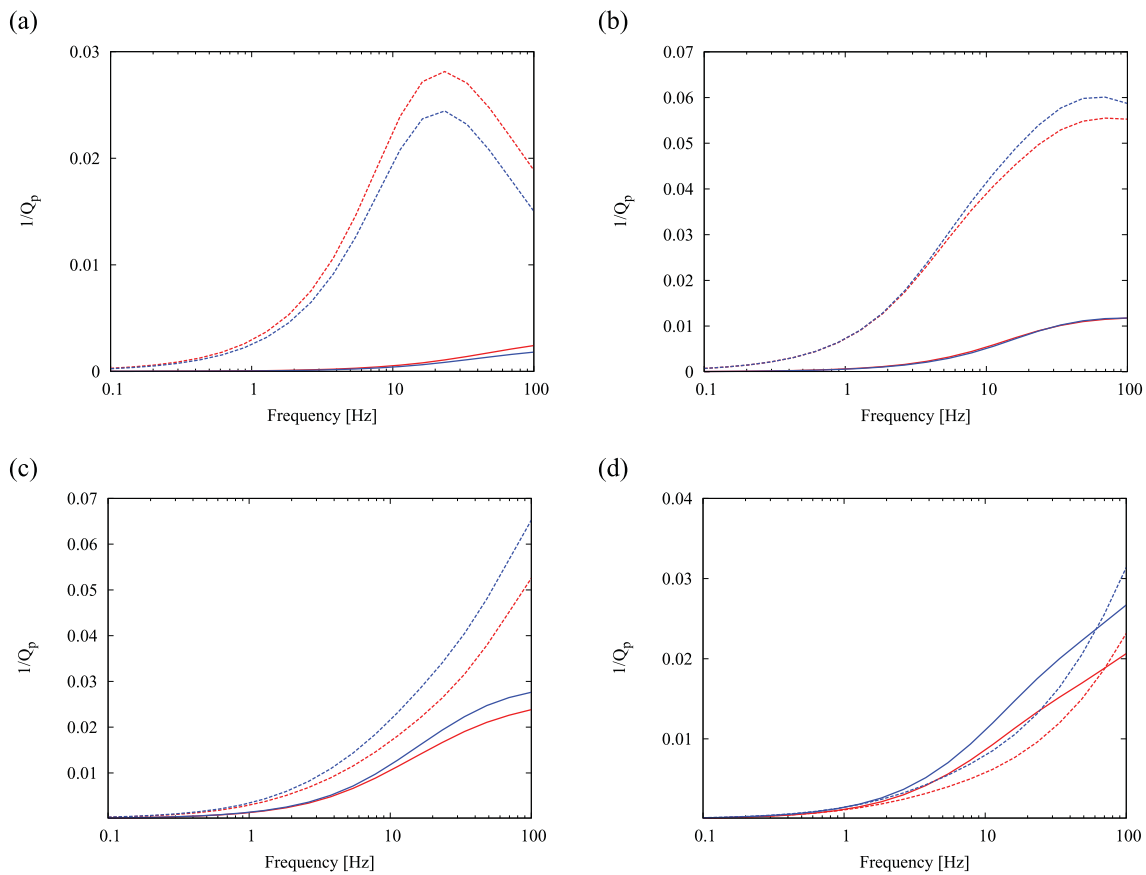
Figure 5. Gas saturation fields obtained from the porosity distribution shown in Fig. 3. The different panels show the saturation patterns corresponding to capillary pressure values of (a) 1.8 KPa, (b) 2 KPa, (c) 2.2 KPa and (d) 2.4 KPa.

Figure 6. Inverse quality factor as a function of frequency for the porosity field shown in Fig. 3 and the saturation distributions shown in Fig. 5. Red and blue lines denote heterogeneous and homogeneous porosity fields, respectively. The corresponding solid and dashed line patterns refer to spatially continuous and patchy-type binary saturation patterns, respectively.

$S_t = 0.05$, because around this value we observe a rapid change in the behaviour of the bulk modulus of the mixture of gas and water as a function of gas saturation. For both spatially continuous and patchy-type binary gas–water distributions, we also consider two subcases: heterogeneous and homogeneous distributions of porosity and all associated physical parameters of the dry frame. In the latter case, we take a constant porosity value equal to the average porosity of the field shown in Fig. 3.

For most cases shown in Figs 6 and 7, we observe that seismic attenuation and velocity dispersion effects for binary patchy gas–water distributions are much more significant than those obtained considering the physically based continuous saturation patterns. These effects are particularly dramatic in cases (b) and (c), with Q-values below 20 for certain frequencies and velocity increases of up to about 5 per cent in the considered frequency range. Very significant discrepancies between the responses considering the two fluid distributions can also take place in the case (a), where for the binary distributions Q-values can be below 50 for certain frequencies. These differences are likely to be due to the fact that in the case considering spatially continuous variations of gas saturation the smoothly spatially varying fluid compressibility produce wave-induced fluid pressure gradients less significant than those taking place in rocks characterized by very abrupt changes in the compressibility of the pore fluid.

As expected, the inferred velocities in the low frequency limit depend strongly on the characteristics of the fluid distributions.

However, this parameter also depends on the characteristics of the dry frame, particularly in the case of the continuous fluid distributions, as can be seen in Fig. 7. Moreover, the rate of change of the phase velocity with respect to frequency depends mainly on the characteristics of fluid distributions.

It is also interesting to note that for the binary fluid distributions the attenuation and phase velocity curves obtained considering the heterogeneous porosity field are quite similar to those for the homogeneous solid frame. The similarities between the responses considering heterogeneous and homogeneous dry frames also exist for the spatially continuous gas–water distributions, particularly in the case of seismic attenuation. These observations suggest that mesoscopic effects in such environments are more sensitive to the heterogeneities associated with the fluid properties than to solid frame heterogeneities. Correspondingly, these results also point to the importance of accounting for the spatially continuous nature of gas–water distributions, if a detailed analysis of seismic attenuation behaviour is required.

To analyse the levels of attenuation and velocity dispersion for different amounts of gas within the rock sample, Fig. 8 shows the phase velocity and inverse quality factor as functions of overall gas saturation for different frequencies and for continuous and binary gas–water distributions. We observe that in the case of spatially continuous saturation patterns the attenuation levels are significant for frequencies of 50 and 100 Hz and mainly for overall gas saturations around 0.01. Moreover, in these cases Q-values are below 100 for
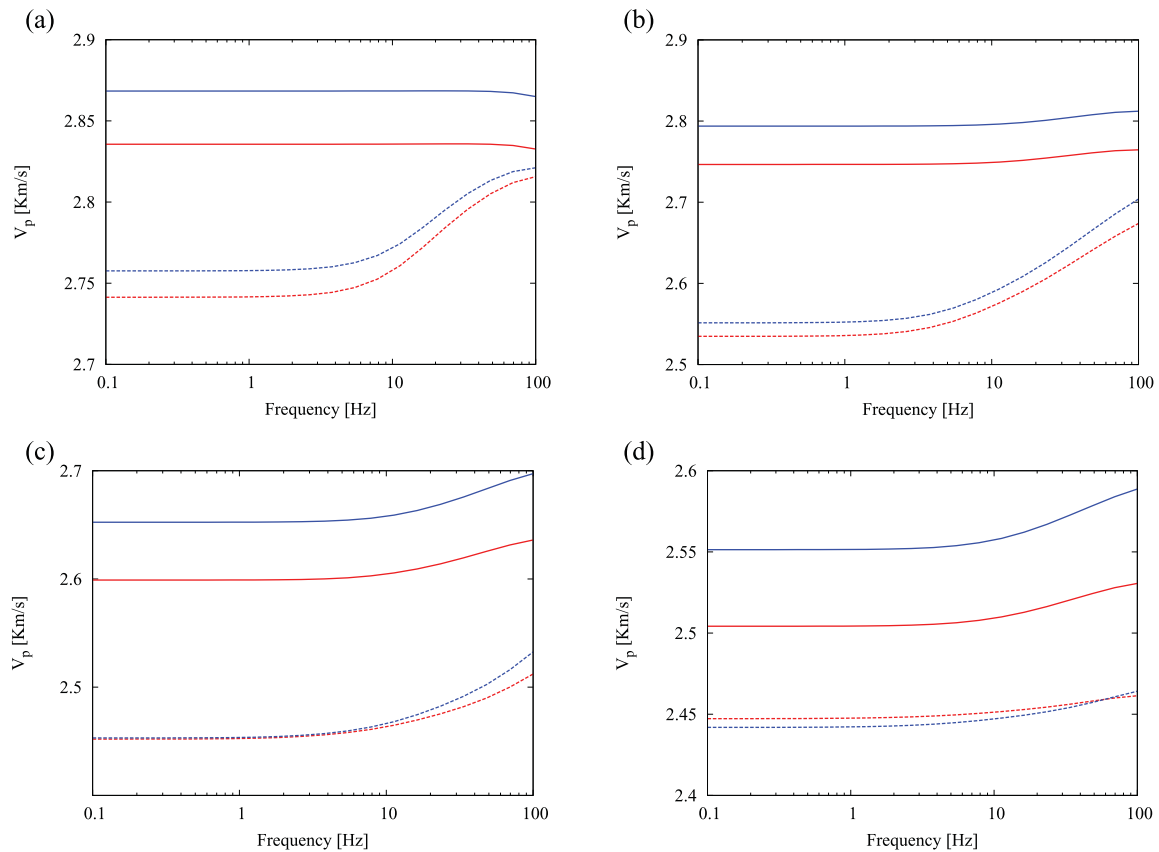
(a)

(b)

(c)

(d)

Figure 7. Compressional phase velocity as a function of frequency for the porosity field shown in Fig. 3 and the saturation distributions shown in Fig. 5. Red and blue lines denote heterogeneous and homogeneous porosity fields, respectively. The corresponding solid and dashed line patterns refer to spatially continuous and patchy-type binary saturation patterns, respectively.

overall saturations below ∼0.05. As expected, we also see that, for a given frequency, the phase velocity decreases with overall saturation for the saturation values shown in Fig. 8. In addition, velocity dispersion prevails for overall gas saturations below ∼0.06, albeit at a not very significant level.

The situation for binary patchy-type saturation patterns is different. We observe much more significant attenuation levels with Q-values even below 20 for overall saturations between 0.01 and 0.05 and frequencies of 50 Hz and between 0.01 and 0.08 for a frequency of 100 Hz. Q-values below 100 are found for the entire saturation range considered and velocity dispersion effects are more significant in this case. It is interesting to note that the phase velocity obtained for a frequency of 1 Hz turned out to be similar to that corresponding to the spatially continuous fluid distributions, which can be explained by the fact that dispersion effects are negligible for such a low frequency together with the fact that the total amount of gas present in the rock sample as well as the dry frame characteristics are similar in both cases.

For overall saturation values higher than those considered in the panels shown in Fig. 8, attenuation and velocity dispersion effects become less significant with increasing overall saturation. However, while such effects turned out to be negligible for the continuous gas–water distributions, they can be very significant for the binary distributions. We obtained Q-values below 100 for saturations up to $\overline{S}_g = 0.25$ for a frequency of 50 Hz and up to $\overline{S}_g = 0.32$ for 100 Hz.

The available evidence therefore suggests that attenuation and velocity dispersion effects produced by wave-induced fluid flow

seem to occur mainly for very low overall gas saturation levels. Moreover, these effects are much more significant and occur over a broader range of saturation level when patchy-type binary, rather than continuous, saturation patterns prevail.

4 PARTIAL SATURATION RELATED TO HETEROGENEOUS CLAY CONTENT DISTRIBUTIONS

The presence of clay affects the mechanical properties of shaly sandstones (e.g. Han *et al.* 1986). Indeed, the distribution of clay minerals in certain parts of the pore structure influences their effects on the dry elastic properties and stress sensitivity of the geological formations (Han *et al.* 1986; MacBeth & Riberio 2007; Mavko *et al.* 2009). Moreover, the presence of clay also has a significant impact on the porosity and permeability of sandstones (e.g. Yin 1993; Han *et al.* 1986) and heterogeneous clay content distributions are therefore expected to result in complex partial gas–water saturation patterns as well as mesoscopic heterogeneities associated with the dry frame properties. In the following, we study wave-induced fluid flow effects in partially saturated shaly sandstones.

To account for the dependency between clay content and porosity, permeability and dry frame elastic moduli, we consider the corresponding laboratory data presented by Yin (1993) and later employed by Knight *et al.* (1998). Fig. 9 shows the porosity, permeability, and dry frame moduli as functions of clay content measured by Yin (1993) for a set of shaly sandstones as well as the
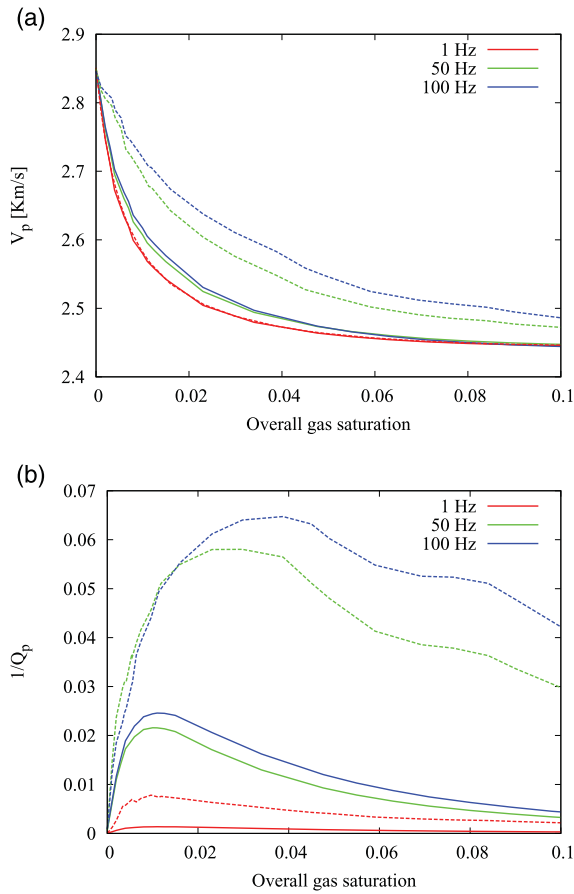
Figure 8. (a) Equivalent phase velocity and (b) inverse quality factor as functions of overall gas saturation obtained using the numerical upscaling procedure and considering the model proposed in this section. The different colours indicate different frequencies, while solid and dashed line patterns refer to spatially continuous and patchy-type binary saturation patterns. In all cases the dry frame properties are determined by the porosity field shown in Fig. 3.

corresponding linear interpolations between the measured values used for our numerical experiments. We observe that there is no significant change of the dry frame elastic moduli with clay content, while the porosity and permeability show significant variations. The latter is particularly important in the context of this work, since permeability fluctuations produced by heterogeneous clay content distributions will produce different gas saturation patterns and therefore different seismic responses.

Since we use Biot's (1956a) model to obtain the response of the rock samples subjected to the compressibility test (Appendix), we treat the mixture of quartz and clay at each computational cell as a single effective medium. The corresponding bulk density of the solid grains of such an effective medium is given by

$$\rho_s = \gamma \rho_c + (1 - \gamma)\rho_q, \qquad (17)$$

where γ is the clay content and ρ_c is the density of the clay grains. To compute the elastic moduli of the solid grains we employ the Voigt-Reuss-Hill average (e.g. Mavko *et al.* 2009),

$$k_s = \frac{1}{2}\left[\gamma k_c + (1 - \gamma)k_q + \left(\gamma/k_c + (1 - \gamma)/k_q\right)^{-1}\right],$$

$$\mu_s = \frac{1}{2}\left[\gamma \mu_c + (1 - \gamma)\mu_q + \left(\gamma/\mu_c + (1 - \gamma)/\mu_q\right)^{-1}\right], \qquad (18)$$
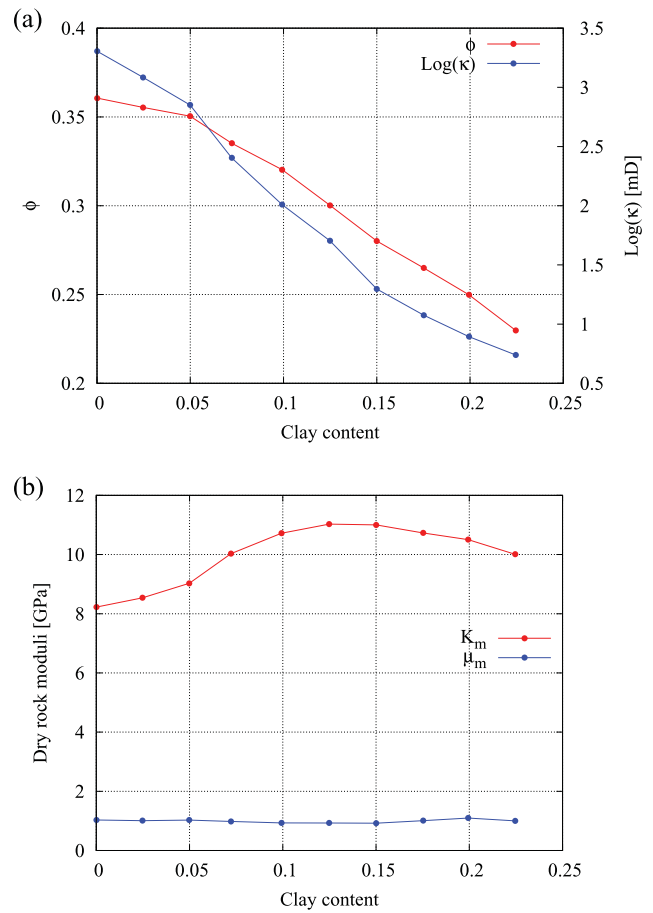

Figure 9. (a) Porosity and permeability as well as (b) dry frame elastic moduli of shaly sandstones as functions of the clay content as measured by Yin (1993) (points) and corresponding linear interpolations (lines) employed to study attenuation and velocity dispersion effects in such media.

where k_c and μ_c are the bulk and shear moduli of the clay particles.

Fig. 10 shows the diffusion length as a function of clay content for a frequency of 100 Hz and considering full gas and full water saturation. To compute this physical parameter, we use eqs (10) and (11). To obtain the various physical properties involved in these equations as functions of clay content, we use linear interpolations of the corresponding laboratory measurements of Yin (1993) (Fig. 9) and the eqs (17) and (18), in conjunction with the values shown in Table 1 for the solid grain properties. We observe that the diffusion length decreases with clay content and that it is smaller in the case fully saturated with gas. It is interesting to note that, regardless of the type of pore fluid, the diffusion lengths are smaller than 1 cm for rocks having clay contents above ∼0.15.

To analyse the wave-induced fluid flow effects in these environments, we consider realistic distributions of clay content within a sand and obtain the corresponding fluid distributions following the model explained before. To obtain the clay content distributions, we again consider stochastic processes governed by a von-Karman-type spectral density function (eq. 15) and allow for volumetric clay content values between 0 and 0.15, which is a reasonable clay content range for most common siliciclastic reservoir rocks (Vernik 1998). Fig. 11 shows the particular clay content field employed in the following analysis, which has a mean of 0.072 and standard deviation of 0.024 and was obtained considering a
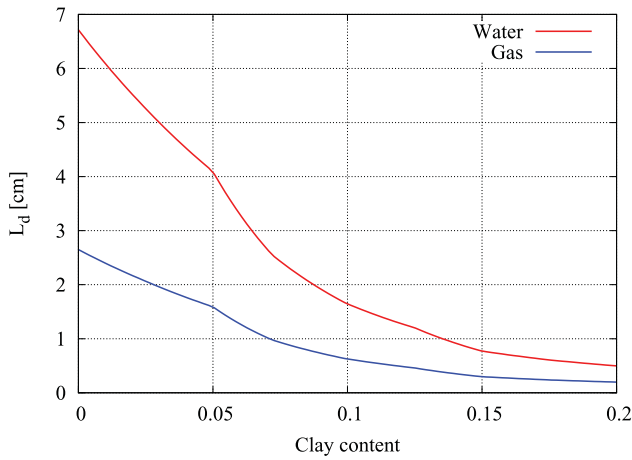
Figure 10. Diffusion length as a function of clay content for the model presented in this section. We consider full water and full gas saturation and a frequency of 100 Hz.
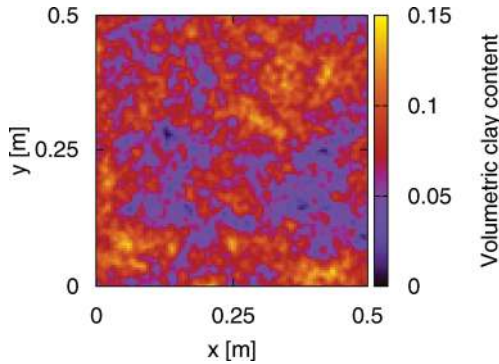

Figure 11. Spatial distribution of the clay content fraction considered to analyse seismic attenuation and velocity dispersion associated with corresponding spatial variations in gas–water saturation. This field has a mean of 0.072 and standard deviation of 0.024.

spatially isotropic correlation length of 0.1 m and $H = 0.1$. The grid spacing considered in this case is of 0.005 m, which is smaller than the diffusion length for clay contents below ∼0.10 (Fig. 10). It is important to note here that we have performed a 1-D convergence analysis to ensure that this grid spacing is indeed small enough to properly represent the pore pressure diffusion processes taking place at the different discontinuities of the media under consideration, and thus, to allow us to observe the corresponding mesoscopic effects.

Fig. 12 shows the saturation patterns obtained considering the clay content distribution shown in Fig. 11 and different capillary pressure values. The overall gas saturations of these samples are (a) 0.004, (b) 0.024, (c) 0.0685 and (d) 0.137. We observe that for low capillary pressure, only the regions with very little clay contain some gas in the pore space (Fig. 12a), while for higher capillary pressures gas also invades the more clay-rich regions.

Fig. 13 shows the inverse quality factor as a function of frequency for the clay content field shown in Fig. 11 and the different gas–water distributions shown in Fig. 12. We see that mesoscopic loss can be significant in these environments, particularly in case (b), where Q-values below 50 can take place in the seismic frequency range. The loss levels are not so significant for the other

capillary pressure values considered in this analysis. However, Q-values below 100 occur for frequencies above 10 Hz in cases (a) and (c), and above ∼35 Hz for the case (d). Fig. 14 shows the corresponding phase velocity as a function of frequency, where we observe velocity dispersion effects, mainly in cases (b) and (c). However, in all cases the relative changes are below 2.1 per cent in the considered frequency range thus indicating that these effects are negligible.

As in the previous section, we also include in Figs 13 and 14 the responses involving spatially continuous and binary patchy-type gas–water distributions with heterogeneous and homogeneous clay content distributions for the rock frame. In the latter case, we take a constant clay content value equal to the average clay content of the field shown in Fig. 11. We observe that also in this case the mesoscopic effects are more significant when considering binary gas–water distributions. This can be clearly observed in Fig. 13(a), where Q-values below 25 are found for the binary distributions. In case (b), attenuation is also more significant in the patchy case for frequencies above ∼20 Hz. Conversely, it is interesting to note that attenuation is slightly less significant for most of the considered frequency range in cases (c) and (d), if binary fluid distributions are considered. We also observe that the velocities in the low frequency limit as well as the rate of change with respect to frequency depend mainly on the characteristics of fluid distributions (Fig. 14).

For binary fluid distributions the attenuation and phase velocity responses obtained considering the heterogeneous clay content distribution are quite similar to those for the homogeneous solid frame. These similarities between the responses considering heterogeneous and homogeneous dry frame properties also occur for the spatially continuous gas–water distributions and suggest that mesoscopic effects in partially saturated shaly sandstones are again more sensitive to the heterogeneities associated with the properties of the pore fluid than to those associated with the solid frame.

Fig. 15 shows the phase velocity and inverse quality factor as functions of overall gas saturation for different frequencies and for continuous and binary gas–water distributions obtained modifying the capillary pressure. We observe that for spatially continuous saturation, the attenuation levels are significant for frequencies of 50 and 100 Hz and for overall gas saturations around 0.03. In addition, in these cases Q-values are below 100 for overall saturations below ∼0.15. The phase velocity decreases with overall saturation, and velocity dispersion effects in the saturation range considered in this analysis turned out to be largely negligible.

The situation for binary saturation patterns is again different. We observe much more significant attenuation levels with Q-values even below 25 for certain overall saturations and frequencies of 50 and 100 Hz. Indeed, for such frequencies, Q-values below 100 are observed for the entire saturation range considered, except for overall saturations close to zero. In the case of a frequency of 1 Hz, we obtained Q-values below 100 for saturations around 0.025. We also note significant velocity dispersion effects within the saturation range considered. As expected, we see that also in this case the phase velocity obtained for a frequency of 1 Hz turned out to be similar to that corresponding to the spatially continuous fluid distributions.

For saturations higher than those considered in Fig. 15, attenuation and velocity dispersion effects become less significant with increasing overall saturation for both types of fluid distributions. However, while such effects turned out to be negligible for the continuous gas–water distributions, they can be very significant for
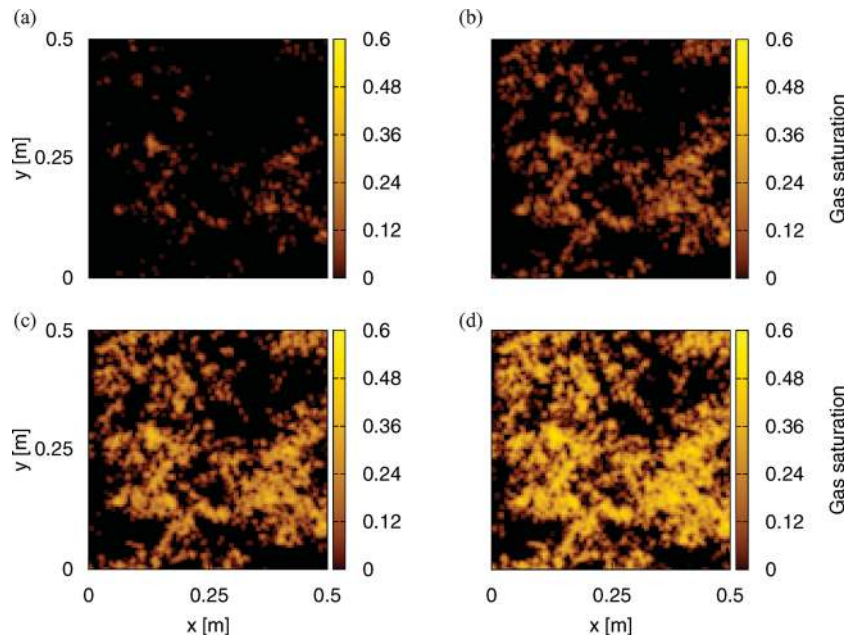
Figure 12. Gas saturation fields obtained from the clay content distribution shown in Fig. 11. The different panels show the saturation patterns corresponding to capillary pressure values of (a) 2.75 KPa, (b) 3.25 KPa, (c) 4 KPa and (d) 5 KPa.
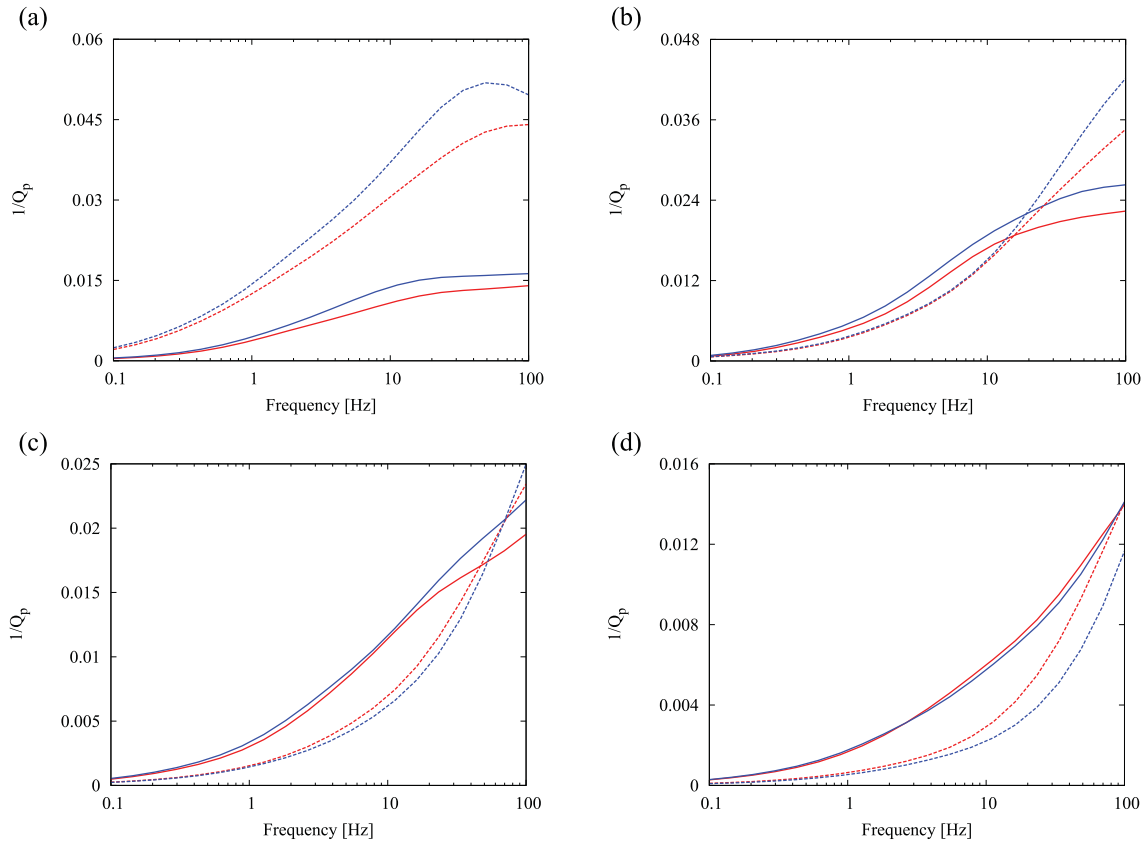

Figure 13. Inverse quality factor as a function of frequency for the clay content field shown in Fig. 11 and the saturation distributions shown in Fig. 12. Red and blue lines denote heterogeneous and homogeneous clay content distributions, respectively. The corresponding solid and dashed line patterns refer to spatially continuous and patchy-type binary saturation patterns, respectively.

Figure 14. Compressional phase velocity as a function of frequency for the clay content field shown in Fig. 11 and the saturation distributions shown in Fig. 12. Red and blue lines denote heterogeneous and homogeneous clay content distributions, respectively. The corresponding solid and dashed line patterns refer to spatially continuous and patchy-type binary saturation patterns, respectively.
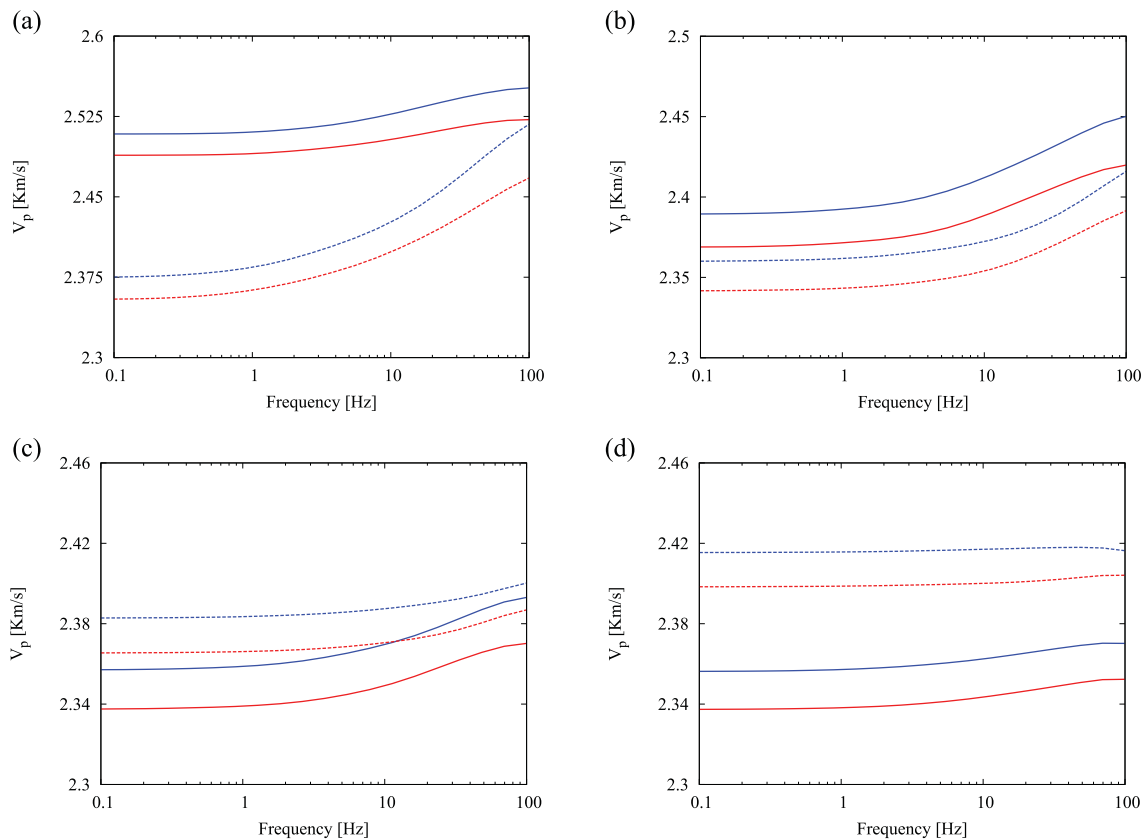
the binary distributions, where we observe Q-values below 100 for saturations up to $\overline{S}_g = 0.5$ at 50 Hz, and up to $\overline{S}_g = 0.6$ at 100 Hz.

5 CONCLUSIONS

We have analysed wave-induced fluid flow effects in porous rocks partially saturated with gas and water. In doing so, we have assumed that the saturation patterns are governed by mesoscopic heterogeneities associated with the dry frame properties due to capillary pressure equilibrium. The multiscale nature of the gas–water distribution was taken into account by determining locally an effective fluid which in turn was then used for the larger-scale simulations. To estimate the seismic attenuation and velocity dispersion of these media we applied a numerical compressibility test, which is a convenient way of accounting for mesoscopic heterogeneities associated with dry frame properties as well as for spatial variations of the physical properties of the pore fluid.

We have performed two sets of numerical experiments, in which the saturation field was determined by realistic variations in porosity and clay content distributions, respectively, and we considered both spatially continuous and binary gas–water distributions as well as heterogeneous and homogeneous rock frames. These numerical examples, which are in many ways representative of our overall findings, let us observe that partial saturation, for both binary patchy-type and spatially continuous gas saturation patterns, may produce significant attenuation and modest velocity dispersion effects, in

particular when relatively small amounts of gas are present in the rock sample. In addition, we found that the seismic responses with regard to attenuation and, to a lesser extent also with regards to phase velocity, are more sensitive to the heterogeneities associated with the fluid properties than to solid frame heterogeneities. These experiments also show that, in most cases, attenuation and velocity dispersion effects are much more significant and occur over a broader saturation range for binary patchy-type gas–water distributions.

The results obtained in this study thus indicate that the nature of gas saturation patterns is a critical parameter controlling the seismic behaviour of porous rocks partially saturated with gas and water. Therefore, rock frame heterogeneities, which do not significantly affect the seismic responses *per se*, should still be taken into account, since they may determine the characteristics of gas–water distributions of the probed formations. Finally, the methodological framework developed in this work may have the potential for improving our understanding of time-lapse seismic data associated with hydrocarbon production or CO_2 injection processes due to the associated capillary pressure changes, which do not only affect the effective stress but also the characteristics of fluid distributions.
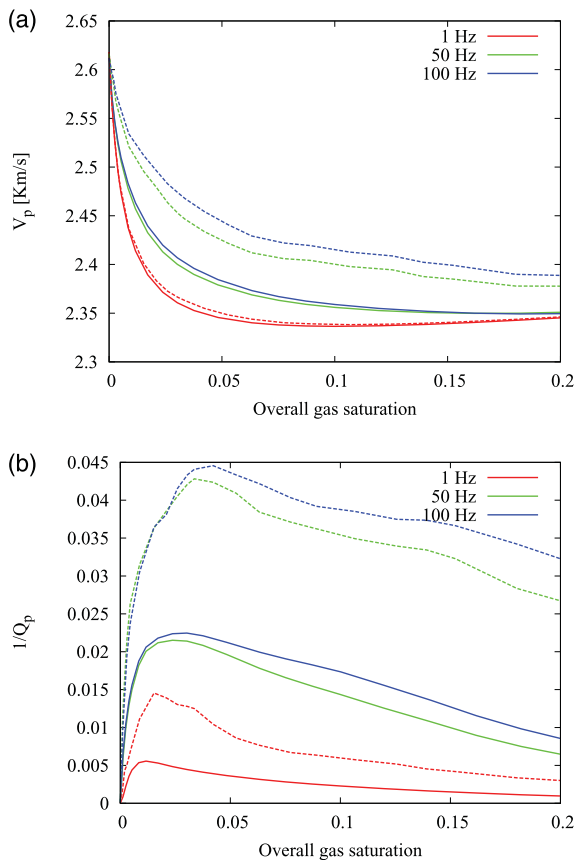
Figure 15. (a) Equivalent phase velocity and (b) inverse quality factor as functions of overall gas saturation obtained using the numerical upscaling procedure and considering the model proposed in this section. The different colours indicate different frequencies, while solid and dashed line patterns refer to spatially continuous and patchy-type binary saturation patterns, respectively. In all cases the dry frame properties are determined by the clay content distribution shown in Fig. 11.

REFERENCES

Berryman, J., 1982. Elastic waves in fluid-saturated porous media, in *Lecture Notes in Physics*, Vol. 154, pp. 28–50, eds. Ehlers, J., Hepp, K., Kippenhahn, R., Weidenmüller, H.A., & Zittart, J., Springer-Verlag, Heidelberg, Germany.

Biot, M.A., 1956a. Theory of propagation of elastic waves in a fluid-saturated porous solid.I. Low frequency range, *J. acoust. Soc. Amer.,* **28,** 168–178.

Biot, M.A., 1956b. Theory of propagation of elastic waves in a fluid-saturated porous solid.II. Higher frequency range, *J. acoust. Soc. Amer.,* **28,** 179–191.

Brooks, R.H. & Corey, A.T., 1964. Hydraulic properties of porous media, Hydrology Paper No. 3, Colorado State University.

Cadoret, T., Marion, D. & Zinszner, B., 1995. Influence of frequency and fluid distribution on elastic wave velocities in partially saturated limestones, *J. geophys. Res.,* **100,** 9789–9803.

Cadoret, T., Mavko, G. & Zinszner, B., 1998. Fluid distribution effect on sonic attenuation in partially saturated limestones, *Geophysics,* **63,** 154–160.

Carcione, J.M. & Picotti, S., 2006. P-wave seismic attenuation by slow-wave diffusion: effects of inhomogeneous rock properties, *Geophysics,* **71,** O1–O8.

Carcione, J.M., Picotti, S., Gei, D. & Rossi, G., 2006. Physics and seismic modeling for monitoring CO_2 storage, *Pure appl. Geophys.,* **163,** 175–207.

Dutta, N.C. & Odé, H., 1979. Attenuation and dispersion of compressional waves in fluid-filled porous rocks with partial gas saturation (White model) - Part I: Biot theory, *Geophysics,* **44,** 1777–1788.

Dvorkin, J. & Nur, A., 1998. Acoustic signatures of patchy saturation, *Int. J. Solids Structures,* **35,** 4803–4810.

Dvorkin, J., Moos, D., Packwood, J.L. & Nur, A., 1999. Identifying patchy saturation from well logs, *Geophysics,* **64,** 1756–1759.

Gurevich, B. & Lopatnikov, S.L., 1995. Velocity and attenuation of elastic waves in finely layered porous rocks, *Geophys. J. Int.,* **121,** 933–947.

Han, D., Nur, A., & Morgan, D., 1986. Effects of porosity and clay content on wave velocities in sandstones, *Geophysics,* **51,** 2093–2107.

Homsy, G.M., 1987. Viscous fingering in porous media, *Annu. Rev. Fluid Mech.,* **19,** 271–311.

Johnson, D.L., 2001. Theory of frequency dependent acoustics in patchy-saturated porous media, *J. acoust. Soc. Amer.,* **110,** 682–694.

Kelkar, M. & Perez, G., 2002. *Applied Geostatistics for Reservoir Characterization,* Society of Petroleum Engineers, Richardson, Texas.

Knight, R., Dvorkin, J. & Nur, A., 1998. Acoustic signatures of partial saturation, *Geophysics,* **63,** 132–138.

Krief, M., Garat, J., Stellingwerff, J. & Ventre, J., 1990. A petrophysical interpretation using the velocities of P and S waves (full waveform sonic), *Log Analyst,* **31,** 355–369.

MacBeth, C., & Ribeiro, C., 2007. The stress sensitivity of shaley sandstones, *Geophys. Prospect.,* **55,** 155–168.

Masson, Y.J. & Pride, S.R., 2011. Seismic attenuation due to patchy saturation, *J. geophys. Res.,* **116,** B03206, doi:10.1029/2010JB007983.

Mavko, G., Mukerji, T. & Dvorkin, J., 2009. *The Rock Physics Handbook: Tools for Seismic Analysis of Porous Media,* 2nd edn, Cambridge University Press, Cambridge, UK.

Müller, T.M. & Gurevich, B., 2005. A first-order statistical smoothing approximation for the coherent wave field in random porous media, *J. acoust. Soc. Amer.,* **117,** 1796–1805.

Müller, T.M., Lambert, G. & Gurevich, B., 2007. Dynamic permeability of porous rocks and its seismic signatures, *Geophysics,* **72,** E149–E158.

Müller, T.M., Toms-Stewart, J. & Wenzlau, F., 2008. Velocity-saturation relation for partially saturated rocks with fractal pore fluid distribution, *Geophys. Res. Lett.,* **35,** L09306, doi:10.1029/2007GL033074.

Müller, T.M., Gurevich, B. & Lebedev, M., 2010. Seismic wave attenuation and dispersion resulting from wave-induced flow in porous rocks—A review, *Geophysics,* **75,** A147–A164.

Norris, A.N., 1993. Low-frequency dispersion and attenuation in partially saturated rocks, *J. acoust. Soc. Amer.,* **94,** 359–370.

Pride, S.R., 2005. Relationships between seismic and hydrological properties, in *Hydrogeophysics,* pp. 253–290, eds. Rubin, Y., & Hubbard, S., Springer, Amsterdam, the Netherlands.

Pride, S.R., Berryman, J.G. & Harris, J.M., 2004. Seismic attenuation due to wave-induced flow, *J. geophys. Res.,* **109,** B01201, doi:10.1029/2003JB002639.

Rubino, J.G., Ravazzoli, C.L. & Santos, J.E., 2009. Equivalent viscoelastic solids for heterogeneous fluid-saturated porous rocks, *Geophysics,* **74,** N1–N13.

Rubino, J.G., Velis, D.R. & Sacchi, M.D., 2011. Numerical analysis of wave-induced fluid flow effects on seismic data: application to monitoring of CO_2 storage at the Sleipner Field, *J. geophys. Res.,* **116,** B03306, doi:10.1029/2010JB007997.

Teja, A.S. & Rice, P., 1981. Generalized corresponding states method for viscosities of liquid mixtures. *Ind. Eng. Chem. Fundam.,* **20,** 77–81.

Thomas, L.K., Katz, D.L. & Tek, M.R., 1968. Threshold pressure phenomena in porous media. *Soc. Petrol. Eng. J.,* **243,** 174–184.

Toms, J., Müller, T.M., Ciz, R. & Gurevich, B., 2006. Comparative review of theoretical models for elastic wave attenuation and dispersion in partially saturated rocks, *Soil Dyn. Earthq. Eng.,* **26,** 548–565.

Toms-Stewart, J., Müller, T.M., Gurevich, B. & Paterson, L., 2009. Statistical characterization of gas-patch distributions in partially saturated rocks, *Geophysics,* **74,** WA51–WA64.

Tronicke, J. & Holliger, K., 2005. Quantitative integration of hydrogeophysical data: conditional geostatistical simulation for characterizing heterogeneous alluvial aquifers. *Geophysics,* **70,** K23–K32.

Vernik, L., 1998. Acoustic velocity and porosity systematics in siliciclastics. *Log Analyst,* **39,** 27–35.

White, J., 1975. Computed seismic speeds and attenuation in rocks with partial gas saturation, *Geophysics,* **40,** 224–232.

White, J., Mikhaylova, N. & Lyakhovitskiy, F., 1975. Low-frequency seismic waves in fluid-saturated layered rocks, *Izvestija Acad. Sci. USSR, Phys. Solid Earth,* **10,** 654–659.

Wood, A.W., 1955. *A Textbook of Sound,* MacMillan Publishing Company, New York, NY.

Yin, H., 1993. Acoustic velocity and attenuation of rocks: Isotropy, intrinsic anisotropy, and stress-induced anisotropy, *PhD thesis*, Stanford University.

APPENDIX: NUMERICAL OSCILLATORY COMPRESSIBILITY TEST

Studying wave-induced fluid flow effects is a difficult task. This is mainly due to the fact that, in the low frequency range, the diffusion process associated with the fluid pressure equilibration is a critical issue because the corresponding diffusion lengths are very small as compared with the seismic wavelengths. Rubino *et al.* (2009) proposed a numerical upscaling procedure by simulating oscillatory compressibility tests on representative rock samples to obtain their equivalent complex undrained plane wave modulus, which contains the information on attenuation and velocity dispersion due to the presence of the mesoscopic heterogeneities. Given the importance of this method for the work presented in this paper, we briefly outline its key aspects in the following.

Following the work by Biot (1956a), the elastic stress-strain relations can be written in the form

$$\sigma_{ij}(u) = 2\mu\,\epsilon_{ij}(u^{\mathrm{s}}) + \delta_{ij}(\lambda_{\mathrm{c}}\,\nabla\cdot u^{\mathrm{s}} + \alpha k_{av}\,\nabla\cdot u^{\mathrm{f}}), \tag{A1}$$

$$p_{\mathrm{f}}(u) = -\alpha k_{av}\,\nabla\cdot u^{\mathrm{s}} - k_{av}\,\nabla\cdot u^{\mathrm{f}}, \tag{A2}$$

where u^{s} denotes the average displacement vector of the solid phase, u^{f} the average relative fluid displacement per unit volume of bulk material, $\epsilon_{ij}(u^{\mathrm{s}})$ the strain tensor of the solid phase, and σ_{ij} and p_{f} the stress tensor of the bulk material and the fluid pressure, respectively. The coefficient μ is the shear modulus of the bulk material and is considered to be equal to the shear modulus of the dry matrix. The remaining parameters, which we consider to be real and frequency-independent, can be computed in terms of the physical properties of the fluid-saturated porous rock as follows (Rubino *et al.* 2009)

$$\alpha = 1 - \frac{k_{\mathrm{m}}}{k_{\mathrm{s}}}, \tag{A3}$$

$$k_{av} = \left(\frac{\alpha - \phi}{k_{\mathrm{s}}} + \frac{\phi}{k_{\mathrm{f}}}\right)^{-1}, \tag{A4}$$

$$k_{\mathrm{c}} = k_{\mathrm{m}} + \alpha^2 k_{av}, \tag{A5}$$

$$\lambda_{\mathrm{c}} = k_{\mathrm{c}} - \frac{2}{3}\mu. \tag{A6}$$

In the absence of body forces, Biot's (1956a) equations of motion stated in the space-frequency domain can be written in the form

$$-\omega^2\rho_{\mathrm{b}}u^{\mathrm{s}} - \omega^2\rho_{\mathrm{f}}u^{\mathrm{f}} = \nabla\cdot\sigma, \tag{A7}$$

$$-\omega^2\rho_{\mathrm{f}}u^{\mathrm{s}} - \omega^2 gu^{\mathrm{f}} + i\omega bu^{\mathrm{f}} = -\nabla p_{\mathrm{f}}, \tag{A8}$$

where ρ_{b} is the bulk density of the fluid saturated porous material and ω is the angular frequency. The mass coupling coefficient g represents the inertial effects associated with dynamic interactions between the solid and fluid phases, while the coefficient b includes the viscous coupling effects between such phases. In the low frequency range, they can be computed as

$$b = \frac{\eta}{\kappa}, \qquad g = \frac{S\rho_{\mathrm{f}}}{\phi}, \qquad S = \frac{1}{2}\left(1 + \frac{1}{\phi}\right), \tag{A9}$$

where η is the fluid viscosity and κ the absolute permeability. The coefficient S is known as the structure or tortuosity factor and computed according to Berryman (1982).

To compute wave-induced fluid flow effects, we consider a representative rectangular rock sample containing mesoscopic-scale heterogeneities. An essential prerequisite of this procedure is that the dimensions of the probed sample are much smaller than the considered wavelengths (Rubino *et al.* 2009). Moreover, the properties of the sample need to be statistically stationary, which implies that the correlation length of the heterogeneities also need to be significantly smaller than the sample size. The rock sample is then subjected to a time-harmonic compression with constant amplitude of the form $\Delta Pe^{i\omega t}$ on its upper boundary and no tangential forces are acting on the boundaries of the sample. The solid is neither allowed to move on the lower boundary nor have horizontal displacements on the lateral boundaries and the fluid is not allowed to flow into or out of the sample.

Denoting by V the original volume of the sample, its complex oscillatory volume change $\Delta V(\omega)$ allows us to define the equivalent undrained complex plane-wave modulus $\overline{M_{\mathrm{c}}}(\omega)$ by using the relation

$$\frac{\Delta V(\omega)}{V} = -\frac{\Delta P}{\overline{M_{\mathrm{c}}}(\omega)}, \tag{A10}$$

which is valid for a viscoelastic homogeneous solid in the quasistatic case.

To estimate this volume change, Biot's equations of motion (eqs A7 and A8) are solved under proper boundary conditions. In this sense, let $\Omega = (0, L_x) \times (0, L_y)$ be a domain in the (x, y)-plane representing the rock sample to be compressed in the test. Set Γ the boundary of Ω, given by $\Gamma = \Gamma^{\mathrm{L}} \cup \Gamma^{\mathrm{B}} \cup \Gamma^{\mathrm{R}} \cup \Gamma^{\mathrm{T}}$, where

$$\Gamma^{\mathrm{L}} = \{(x, y) \in \Gamma : x = 0\}, \quad \Gamma^{\mathrm{R}} = \{(x, y) \in \Gamma : x = L_x\},$$

$$\Gamma^{\mathrm{B}} = \{(x, y) \in \Gamma : y = 0\}, \quad \Gamma^{\mathrm{T}} = \{(x, y) \in \Gamma : y = L_y\}.$$

Also, denote by ν the unit outer normal on Γ and let χ be a unit tangent on Γ so that $\{\nu, \chi\}$ is an orthonormal system on Γ. Then, to estimate the volume change $\Delta V(\omega)$, we consider the solution of eqs (A7) and (A8) under the following boundary conditions

$$\sigma(u)\nu = (0, -\Delta P), \quad (x, y) \in \Gamma^{\mathrm{T}}, \tag{A11}$$

$$\sigma(u)\nu \cdot \chi = 0, \quad (x, y) \in \Gamma^{\mathrm{L}} \cup \Gamma^{\mathrm{R}}, \tag{A12}$$

$$u^{\mathrm{s}} \cdot \nu = 0, \quad (x, y) \in \Gamma^{\mathrm{L}} \cup \Gamma^{\mathrm{R}}, \tag{A13}$$

$$u^{\mathrm{s}} = 0, \quad (x, y) \in \Gamma^{\mathrm{B}}, \tag{A14}$$

$$u^{\mathrm{f}} \cdot \nu = 0, \quad (x, y) \in \Gamma. \tag{A15}$$

The vertical displacements $u_2^s(x, L_y, \omega)$ on Γ^T allow us to obtain an average vertical displacement $u_2^{s,T}(\omega)$ experienced by the boundary Γ^T. Then, for each frequency ω, the volume change produced by the compressibility test can be approximated by $\Delta V(\omega) \approx L_x u_2^{s,T}(\omega)$, which enables us to compute the equivalent complex plane-wave modulus $\overline{M}_c(\omega)$ through relation (A10). The corresponding complex compressional velocity is given by

$$V_{pc}(\omega) = \sqrt{\frac{\overline{M}_c(\omega)}{\overline{\rho_b}}}, \tag{A16}$$

where $\overline{\rho_b}$ is the average bulk density of the rock sample. The equivalent compressional phase velocity $V_p(\omega)$ and inverse quality factor $Q_p(\omega)$ are then given as

$$V_p(\omega) = \left[\mathrm{Re} \left(\frac{1}{V_{pc}(\omega)} \right) \right]^{-1}, \tag{A17}$$

$$\frac{1}{Q_p(\omega)} = \frac{\mathrm{Im}(V_{pc}(\omega)^2)}{\mathrm{Re}(V_{pc}(\omega)^2)}. \tag{A18}$$

To estimate the equivalent complex moduli, we employ a finite element procedure to approximate the solution of eqs (A7) and (A8) under the corresponding boundary conditions (eqs A11 to A15). We use bilinear functions to approximate the solid displacement vector and a closed subspace of the vector part of the Raviart-Thomas-Nedelec space of zero order for the fluid displacement.